AIAA 2011-2350

Experimental Investigation on the Influence of Sidewall Compression on the Flowfield of a Scramjet Inlet at Mach 7

Oliver M. Hohn[1] and Ali Gülhan[2]
Supersonic and Hypersonic Technology Department, Institute of Aerodynamics and Flow Technology
German Aerospace Center (DLR), Linder Höhe, 51147 Cologne, Germany

In this paper, we present the results of an extensive measurement campaign to investigate the effect of external and internal sidewall compression as well as different contraction ratios on the performance of the flowfield of a scramjet inlet. Experiments were conducted in the H2K windtunnel of the DLR Cologne. The results show that external sidewall compression induces strong separation and vortex structures in the external part which impair the starting behaviour and inhibit any gains of the compression ratio. With internal sidewall compression, strong increases of the pressure ratio could be achieved and the inlet still started at internal contraction ratios well above the Kantrowitz-Limit.

Nomenclature

A	=	area
C_p	=	specific heat capacity at constant pressure
C_v	=	specific heat capacity at constant volume
I	=	internal compression
M	=	Mach number
$\dot{m}$	=	mass flow
MCR	=	mass capture ratio
p	=	pressure
R	=	specific gas constant for air, $R = 287.15$ J kg^{-1} K^{-1}
St	=	Stanton number
T	=	temperature
t	=	time
α	=	heat transfer coefficient or calibration factor
γ	=	ratio of specific heats
Δ	=	throttle degree
η	=	kinetic energy efficiency
λ	=	heat conductivity
π	=	total pressure ratio
ρ	=	density

Subscripts:

D	=	throttle
rec	=	recovery
st	=	static
$t0$	=	wind tunnel total conditions
∞	=	wind tunnel free stream conditions

[1]PhD Student, Wind Tunnel Department of the Institute of Aerodynamics and Flow Technology, German Aerospace Center (DLR), Linder Höhe, 51147 Köln, Germany. Student AIAA Member.
[2] Head of Department, Wind Tunnel Department of the Institute of Aerodynamics and Flow Technology, German Aerospace Center (DLR), Linder Höhe, 51147 Köln, Germany. AIAA Member.

I. Introduction

IN recent years the development of advanced space vehicles has focused on hypersonic airbreathing propulsion, especially on scramjets where, as opposed to regular ramjets, combustion takes place at supersonic speeds. The present study is the latest of a long history of scramjet inlet investigations that are performed at the DLR Cologne. It is also a part of the research training group GRK 1095/2, in which a considerable part of scramjet research activities at several institutions in Germany are concentrated [1].

The subject of this paper is the experimental analysis of the effects that the addition of sidewall compression has on the flowfield of the inlet GK-01 of the GRK scramjet configuration, which is a two-dimensional mixed compression inlet. This is also supposed to gather preliminary data for the future development of a new, completely three-dimensional inlet. A similar approach at the DLR Cologne has already been pursued by Gruhn [2] for the design of the inlet for the Lapcat II configuration.

The inlet of a scramjet engine must ensure the supply of the combustion chamber with a sufficient mass flow of air at the conditions required for supersonic combustion at any time and is therefore crucial to the performance of the whole inlet [3]. In 2D-, mixed compression inlets, the airflow is compressed by oblique shocks from one or more ramps and the lip in both the external and internal part of the inlet flow path. This is a very common type of inlet and has also been the subject of various other projects at the DLR Cologne [4, 5, 6, 7]. However, this type of inlet also brings several disadvantages. Due to the location of the shock waves, very long ramps are necessary to achieve the required compression ratios. Therefore, the focus of research efforts over the last years has shifted to three-dimensional inlets, where compression occurs not only in vertical planes by the ramp and lip shocks but also in horizontal planes by the use of converging sidewalls. Heiser and Pratt [3] list several enhancements that can be achieved with 3D-inlets. They allow for a more compact and thus lighter design and improved starting characteristics as well as less separation. Examples of 3D-inlets are sidewall-compression inlets where compression in horizontal planes only occurs by the forebody and the sidewall compression takes place independently. This type of inlet was extensively examined by Holland both computationally and experimentally [8, 9]. Goonko et. al., on the other hand, investigated 3D-inlets with a single ramp and converging sidewalls [10, 11]. Further types of 3D-inlets are streamtraced inlets, like REST-inlets with a transition from a rectangular capture area to an elliptical combustion chamber [12, 13].

A study to increase the internal compression by additional sidewall compression through wedge inserts in the isolator part of the inlet has already been performed by Häberle [14]. The investigation showed that an increase in the pressure ratio of the inlet was possible but comes at the price of increased total pressure losses.

In contrast to this, the influence of additional sidewall compression by swept wedge inserts in the external part of the inlet has been examined in the current study. A comparison of the different types of inserts is shown in Figure 1. There are two sets of inserts for each configuration so that the throat width can be reduced from 100 mm to 80 mm and 70 mm, respectively.

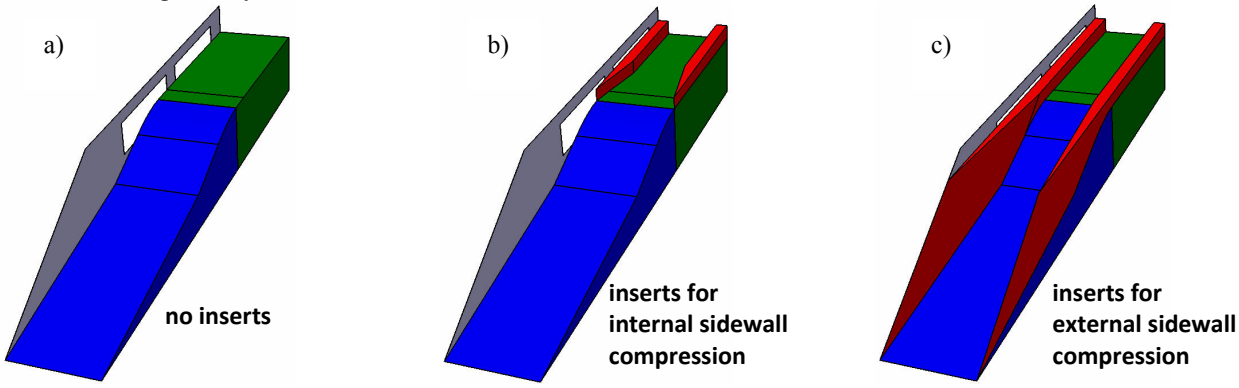

Figure 1. Comparison of different configurations

Preliminary investigations for external sidewall compression showed, however, that the interaction of the sidewall shocks with the ramp shocks pushes the ramp shocks upwards and causes a strong increase in spillage. This inhibits any gains from the additional compression, i.e. no increase in the pressure ratio, but a strong decrease in the mass flow as well as lower pressure recovery. CFD-simulations suggest that by elongating the cowl lip, the goal of a higher pressure ratio with only small additional total pressure losses and no decrease of the mass flow can be

achieved. Therefore, several exchangeable lips were designed so that the inlet can be analyzed with different lip positions and consequently different internal contraction ratios. A detailed description of the various configurations is given in the next section.

Even in a 2D-inlet, the flow path is very complex and contains various flow phenomena, such as shock-shock and shock-boundary-layer interaction, boundary layer separation or the formation of vortices. In the 2D-configuration, the shock of the second ramp causes a separation bubble in the kink between the first and the second ramp. At this point, transition from laminar to turbulent flow occurs as well. However, over the expansion surface between the second ramp and the isolator, the flow relaminarizes again [18, 23]. Consequently, depending on the lip position, the lip shock will hit the boundary layer on the lower wall in a more or less relaminarized state. The shock-boundary-layer interaction at this position causes a large separation bubble which was observed to be of a magnitude of about one third of the throat height of the inlet [15]. Of course, the size of this separation bubble very much depends on the state of the boundary layer. A more relaminarized state would be more likely to separate than a more turbulent state. Therefore, it is expected that less separation would occur on the lower wall in the throat section by the interaction with the lip shock. After this separation zone, the flow is assumed to be turbulent throughout the isolator.

While the elongation of the lip could lead to less separation on the lower wall, the movement of the second ramp shock underneath the cowl could cause more separation on the upper wall. As there already is a separation bubble generated at the upper wall by the separation shock of the separation bubble on the lower wall, there is the risk that these two shocks could create one very big separation zone on the upper wall which could cause the blockage of the inlet. To see, if it is still possible to operate this inlet under stable conditions if the second ramp shock is swallowed by the lip, is one of the goals of this measurement campaign, as this could actually be a very useful feature since the hot mass flow, that is generated in the separation zone induced by the shock-boundary layer interaction of the second ramp shock could also be used for ignition in the combustion chamber.

Another issue is vorticity. Vortices are always present in an inlet flowfield, especially in the corner region of the ramp and the sidewalls. This corner flow is even more complicated by the sidewall compression inserts. The interaction of the ramp shock and the sidewall shocks cause a complex structure including the formation of a bridging shock wave and shock reflections towards the walls. The transitional behaviour is also strongly influenced by the sidewall shocks. A detailed description of the flow structure in a 3D-inlet with swept sidewall leading edges is given by Goonko [11].

II. Experimental Setup

A. Wind Tunnel and Test Conditions

All of the experiments presented in this paper have been conducted in the Hypersonic Windtunnel H2K at the German Aerospace Centre in Cologne. This facility is a blow down wind tunnel designed to simulate Mach numbers of 5.3, 6, 7, 8.7 and 11.2 at Reynolds numbers in the range of $2.5 - 20 \cdot 10^6$ m^{-1} [16]. Depending on the flow condition, test durations of up to 30 s can be achieved. A sketch of the H2K and its performance map are shown in Figure 2 and 3. The current experimental campaign was performed at a Mach number of $M = 7$. The test conditions are listed in Table 1.

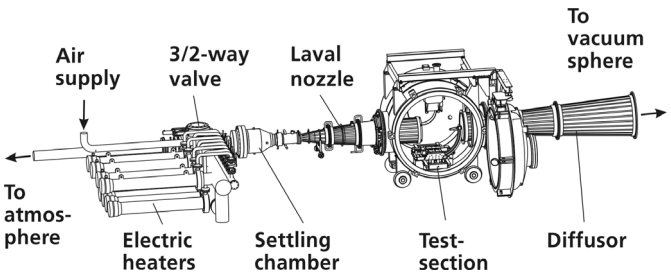

Figure 2. Schematic Drawing of H2K

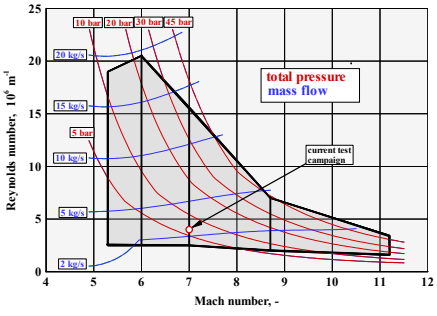

Figure 3. Performance Map of H2K

total temperature T_{t0}, K	500
total pressure p_{t0}, Pa	$7.0 \cdot 10^5$
freestream Mach number M_∞, -	7
freestream pressure p_∞, Pa	170
freestream temperature T_∞, K	46
freestream density ρ_∞, kg m^{-3}	0.0123
unit Reynolds number $Re_{\infty,m}$, -	$4.0 \cdot 10^6$

Table 1. Wind tunnel condition

B. Inlet Model

For all of the experiments, an existing inlet model, designated as GK-01, was used. It is a two-dimensional two-ramp inlet with sidewalls, designed for a flight Mach number of $M = 7.5$. The ramp angles of the GK-01 model are $\delta_1 = 9°$ and $\delta_2 = 20.5°$ to the x-axis. The length of the inlet from the leading edge to the defined interface with the combustion chamber is $L = 0.585$ m. The capture area of the inlet is $A_0 = 0.01$ m^2. The inlet was designed was designed by a computer program using the method of characteristics (MOC) as described by Anderson [17]. A schematic sketch of the inlet is shown in Figure 1 and a picture of the model with sidewall inserts mounted in the H2K in Figure 5. The inlet does not feature any movable parts and thus has to be self starting. To ensure this, the inlet has an optional passive boundary layer bleed in the throat section. Investigations by Häberle showed that the bleed was not necessary [18] and thus the bleed was not used in the present study.

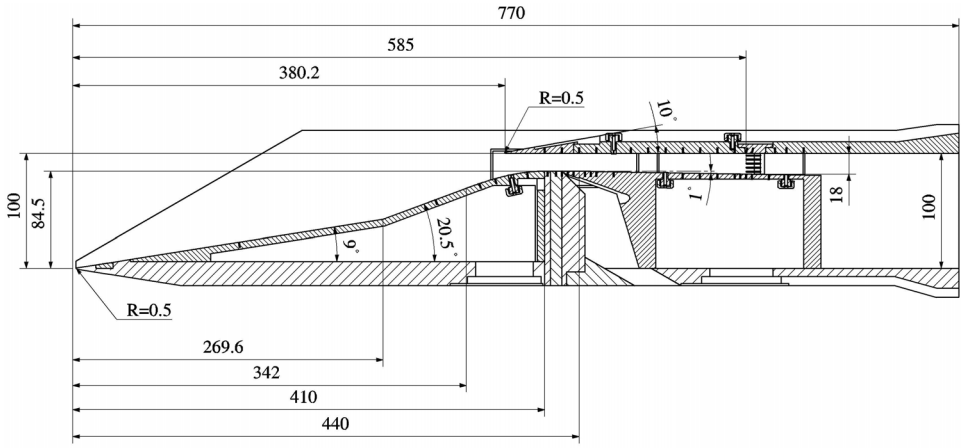

Figure 4. Side view of inlet model GK-01

The sidewall compression inserts are designed to decrease the throat width of the inlet from 100 mm to 70 mm and 80 mm, respectively. The inserts for increased internal contraction start at the end of the expansion surface, i.e. at x = 410 mm from the leading edge. The converging part of the inserts is 90 mm long, resulting in wedge angles of $\delta_{70,int} = 9.5°$ and $\delta_{80,int} = 6.3°$, respectively. The new inserts for external sidewall compression have a sweep angle of 30°. The converging part of the inserts ends at the beginning of the expansion surface, i.e. at x = 342 mm. This yields sidewall compression angles of $\delta_{70,ext} = 3.5°$ and $\delta_{80,ext} = 2.7°$. Due to constructive reasons, the width of the capture area had to be reduced by 1 mm to 99 mm.

The position of the cowl lip is x = 380 mm in the basic configuration. With the modification introduced for this study, it can be extended in steps by up to 40 mm and thus has a severe impact on the internal contraction ratio of the inlet. An overview

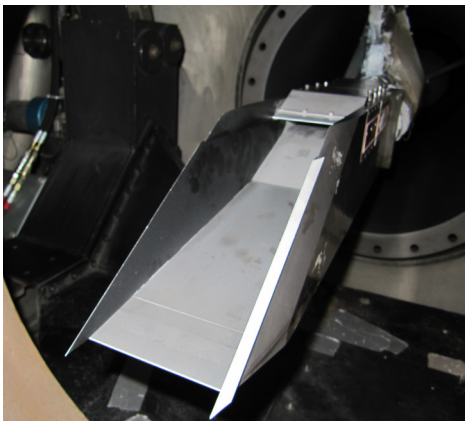

Figure 5. GK-01 with 3D-inserts in the H2K test section

of the different lip positions that were examined, as well as the internal contraction ratios $I = A^*/A_2$ and overall contraction ratio $CR = A_1/A^*$ is given in Table 2.

Configuration	*CR*	Internal contraction *I* for lip position						
		380	375	360	355	350	345	340
No inserts	6.45	0.840	0.798	0.672	0.634	0.598	0.564	0.533
80 mm inserts for external compression	7.98	0.838	0.794	0.664	0.624	0.587	0.552	0.519
70 mm inserts for external compression	9.12	0.836	0.791	0.657	0.617	0.578	0.543	0.510
80 mm inserts for internal compression	7.58	0.716	n/a	0.572	n/a	0.509	n/a	n/a
70 mm inserts for internal compression	8.65	0.626	n/a	0.501	n/a	0.445	n/a	n/a

Table 2. Overview of contraction and internal compression ratios

Since the GK-01 inlet does not feature any starting mechanism, only self-starting configurations can ensure the safe operation of this inlet. The starting ability of an inlet depends on its internal contraction ratio. One criterion for the starting ability is the Kantrowitz limit [19]. Once an inlet is started, the theoretical operational limit is the isentropic contraction ratio. As Figure 6 shows, several of the configurations are well below the Kantrowitz limit and thus might not be self-starting. However, this criterion is not a very strong measure, as it was originally derived for the configuration of the transition from supersonic to subsonic flow in a supersonic diffuser.

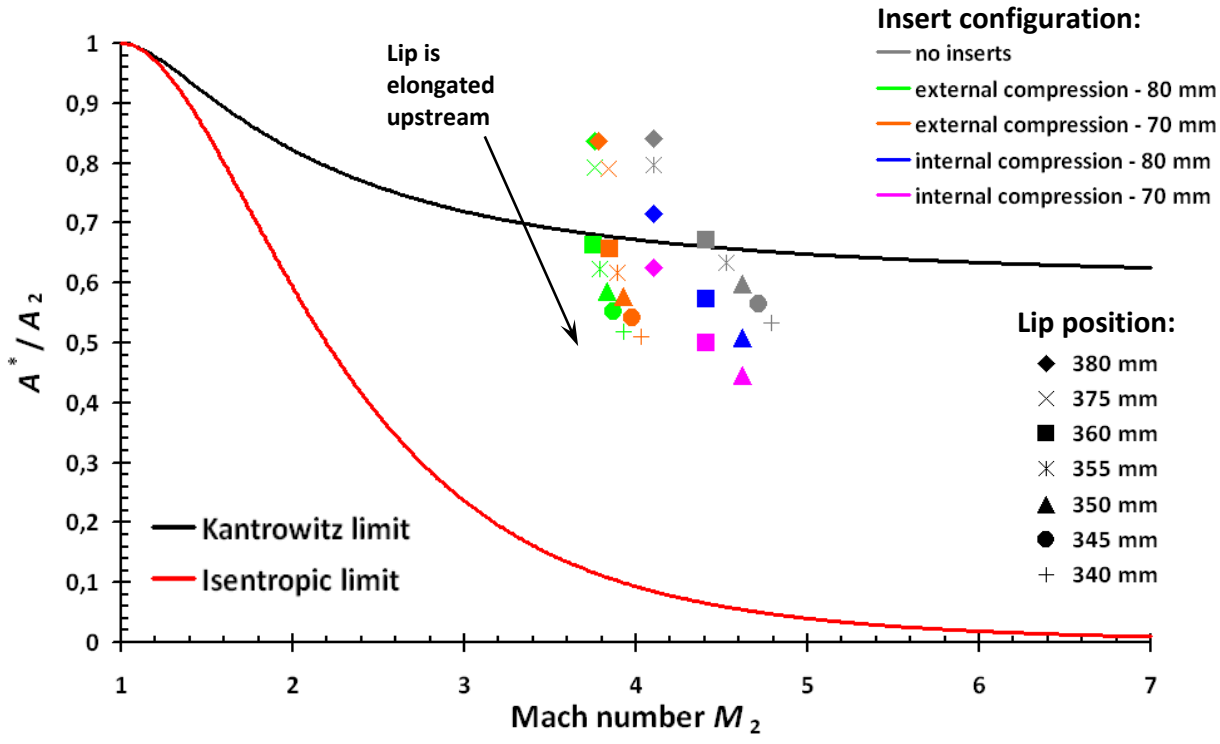

III. Measurement Techniques

A. Optical Diagnostics

Four optical windows in the sidewalls allow optical access to the isolator part of the inlet model, as pointed out in Figure 4. These can either be equipped with silica glasses for flow visualization, or, using PEEK and zinc sulphide inserts, to measure the heat loads on the side walls with infrared thermography. The measurement procedure for the IR-thermography is described later on.

For flow visualization, a coincidence Schlieren system is installed at the hypersonic wind tunnel H2K of the DLR Cologne. During this investigation, the system was used in shadowgraph mode.

B. Pressure and Mach Number Measurements

The inlet model is equipped with 42 static pressure ports along the centreline of the inlet, of which 25 are located on the lower and 17 on the upper wall. Furthermore, a Pitot rake with five Pitot tubes distributed over the height of the isolator is integrated on the centreline at the proposed interface of the isolator and the combustion chamber, i.e. at x = 585 mm from the leading edge of the inlet. This Pitot rake can be shifted 25 mm to the left and right of the centreline. A commercial Pressure Systems Inc. 8400 system using a 32-PSI module was used for the pressure measurements. Both the results of the static and Pitot pressure measurements are displayed as pressure ratios with regard to the free stream total pressure. The accuracies in the determination of the pressure ratios have been calculated to range from ±3.8-5.6% for static and ±3.4-3.8% for Pitot pressures. The results from the Pitot pressure measurements are also used to calculate the Mach number of the flow at the entrance to the combustion chamber. For this procedure, it has to be differentiated between supersonic and subsonic flow. For supersonic flow, the ratio of Pitot and static pressure $p_{Pitot}/p_{st} \leq 1.8939$ and for subsonic flow, $p_{Pitot}/p_{st} > 1.8939$. In the first case, the Mach number can be calculated directly by

$$M_{Pitot} = \sqrt{\frac{2}{\gamma - 1}\left[\left(\frac{p_{Pitot}}{p_{st}}\right)^{\frac{\gamma-1}{\gamma}} - 1\right]} \tag{1}$$

In the second case, the Mach number has to be determined iteratively by solving equation 2:

$$\frac{p_{Pitot}}{p_{st}} = \left(\frac{(\gamma+1)^2 M_{Pitot}^2}{4\gamma M_{Pitot}^2 - 2(\gamma-1)}\right)^{\frac{\gamma}{\gamma-1}} \frac{1-\gamma+2\gamma M_{Pitot}^2}{\gamma+1} \tag{2}$$

The determination of the accuracy for this procedure is quite difficult since it is not possible to measure the static pressure directly at the Pitot tube but instead, the pressure from the nearest wall pressure port hast to be used. Assuming a variation of the static pressure of ±10% over the height of the isolator at the place of the Pitot rake results in a relative error of the Mach number of ±5-6%. However, experience showed that while this assumption is valid for most of the experiments, the variation of the static pressure can be significantly higher in some cases, especially when the isolator flow is already partially subsonic or a shock is present in between the Pitot tube and the static pressure port that is being used.

The Pitot pressure measurements are further used to determine the total pressure recovery π as well as the kinetic energy efficiency η_{ke} of the inlet, which are defined as

$$\pi = \frac{p_{t,Pitot}}{p_{t0}} \tag{3}$$

$$\eta_{ke} = 1 - \frac{2}{(\gamma-1)M_\infty^2}\left[\left(\frac{1}{\pi}\right)^{\frac{\gamma-1}{\gamma}} - 1\right] \tag{4}$$

C. Mass Flow Determination

During the tests, the inlet is mounted on a conical throttle, which is used to simulate the backpressure of the combustion chamber, and also serves as a mass flow meter. Assuming a one-dimensional flow and sonic condition in the throat of the throttle, the mass flow can be calculated with the procedure from Triesch and Krohn [20].

The mass capture ratio if the inlet is defined as

$$m_{CR} = \alpha \frac{\dot{m}_{inlet,exit}}{\dot{m}_0}, \tag{5}$$

where α is a calibration factor determined by calibrating the device according to DIN-1952 [21]. In the concerning region of interest, the values of this factor vary between $0.99 < \alpha < 1.02$. The smallest cross-section area of the throttle, designated by index 4, is calculated with the position of the conical and the geometric dimensions of the throttle by

$$A_{D,th} = \pi \cdot s \cdot \left(r_H + r_4\right). \tag{6}$$

The Mach number in the settling chamber before the throttle (position 3) can then be determined by iteratively solving equation 5:

$$\frac{A_{D3}}{A_{D,th}} = \frac{1}{M_{D3}} \left(\frac{1 + \frac{\gamma - 1}{2} M_{D3}^2}{\frac{\gamma - 1}{2}} \right)^{\frac{\gamma+1}{2(\gamma-1)}} \tag{7}$$

Using the static pressure measured before the throttle (at position 3), the mass flow can be calculated with the total temperature T_{t0} and M_{D3} by

$$\dot{m}_D = \frac{p_{D3}}{\sqrt{RT_{t0}}} A_{D3} \sqrt{\gamma} M_{D3} \sqrt{1 + \frac{\gamma - 1}{2} M_{D3}^2} \ . \tag{8}$$

The static pressure pD3 is taken as the average value of four pressure ports located around the settling chamber of the throttle. With the mass flow going through the capture area A_0 of the inlet, which can be calculated by the free stream conditions of the wind tunnel, the mass flow ration according to equation 3 can the be determined. The accuracy of this method is in the range of ±3%.

Besides the use as a mass flow meter, the throttle also has the important task of imposing a backpressure on the inlet and thus simulation pressure fluctuations in the combustion chamber of a scramjet inlet. This is achieved by lateral movement of the conical plug of the throttle and thus changing the throat area of the throttle as described by equation 4. This is expressed by the throttle degree Δ, defined as

$$\Delta = \left(1 - \frac{A_{D,th}}{A_0}\right) \cdot 100 \tag{9}$$

For the backpressure ratio, which is used in the following discussion, the static pressure at the location of the Pitot rake is used, where the proposed interface of the inlet and combustion chamber is located.

D. Wall Heat Flux Measurements

The determination of wall heat fluxes is a very important task in the design of scramjet engines, especially for the selection of cooling mechanisms as well as materials. In this investigation, heat flux measurements of the sidewalls of the internal flow path as well as the external ramps have been conducted. For the evaluation of the heat fluxes, the chronological development of the surface temperature distribution of the model was recorded with an infrared camera. At the DLR Cologne, a FLIR Systems ThermaCAM SC-3000 is used for this [22]. This camera can be mounted inside of the wind tunnel in an aluminium housing.

The recorded surface temperature data can then be used as the boundary condition for the numerical integration of the nonlinear, one-dimensional heat equation. A detailed description of this procedure can be found in [6]. Here, only the basic equations are displayed in equations 8 and 9, with temperature dependent material properties:

$$\rho(T)c_V(T)\frac{\partial T}{\partial t} = \frac{\partial}{\partial n}\left(\lambda(T)\frac{\partial T}{\partial n}\right) \tag{10}$$

$$\rho(T)c_V(T)\frac{\partial T}{\partial t} = \frac{\partial\lambda(T)}{\partial n}\frac{\partial T}{\partial n} + \lambda(T)\frac{\partial^2 T}{\partial n^2} \Rightarrow \rho(T)c_V(T)\frac{\partial T}{\partial t} = \frac{\partial\lambda(T)}{\partial T}\left(\frac{\partial T}{\partial n}\right)^2 + \lambda(T)\frac{\partial^2 T}{\partial n^2} \tag{11}$$

In order that this one-dimensional approach is valid, there should not be any significant heat fluxes in the plane of the observed surface. This is achieved by the use of a material with very low heat conductivity, PEEK®. This material ensures that the temperature gradient perpendicular to the surface is dominant, and those within the surface plane can be neglected. The temperature dependent material properties are provided by the Institute of Material Science of the German Aerospace Center in Cologne and well known, and thus guarantee sufficient accuracy.

Once the convective wall heat fluxes have been determined, the dimensionless Stanton can be determined by

$$St = \frac{\dot{q}_{conv}}{\rho_\infty u_\infty c_{p,air}(T_{rec} - T_{w)}}\,. \tag{12}$$

With the recovery factor $r = 0.9$ the recovery temperature T_{rec} is defined by

$$T_{rec} = \left(1 + r\frac{\gamma - 1}{2}M_\infty^2\right)T_\infty\,. \tag{13}$$

An analysis of all uncertainties of this procedure resulted in maximum errors of ±5% for the heat fluxes and ±20% for the Stanton number.

IV. Results

A. Starting Behaviour and Flowfield on External Ramps

As mentioned above, some of the configurations that were tested featured an internal contraction ratio that was significantly below the Kantrowitz-criterion for self-starting. As opposed to the expectations the configurations with additional external sidewall compression did not deliver an improved starting behaviour. The inlet did not start for lip positions smaller than 360 mm for the case with 80 mm inserts and 375 mm for the 70 mm inserts. In contrast to that, all other investigated configurations did start, i.e. the inlet started during all test runs where no inserts or additional internal compression was used.

The experimental results by themselves do not give any insight into the reason for this, as no flow visualization is available for these cases. However, related computational examinations by Nguyen et. al. [23] show that the interaction of the sidewall shocks with the shock of the second ramp causes a very large separation bubble in the kink between the first and the second ramp develops, which reaches far upstream on the second ramp and only reattaches for a small area on the second ramp. Furthermore, there is strong formation of corner vorticity as well as a very large vortex in the centre part of the inlet. These effects also create a very thick boundary layer on the second ramp and thus strongly increase the effective internal contraction of this inlet, which presumably also reduces its ability for self starting. For detailed results, please refer to the corresponding paper.

However, as Figure 7 a) and b) show, the measurements of the surface temperature and the subsequent derivation of the Stanton number distribution do support the observations from these simulations. As Häberle [18] and Neuenhahn [24] showed for the 2D-case, there is a separation bubble in the kink between the first and second ramp.

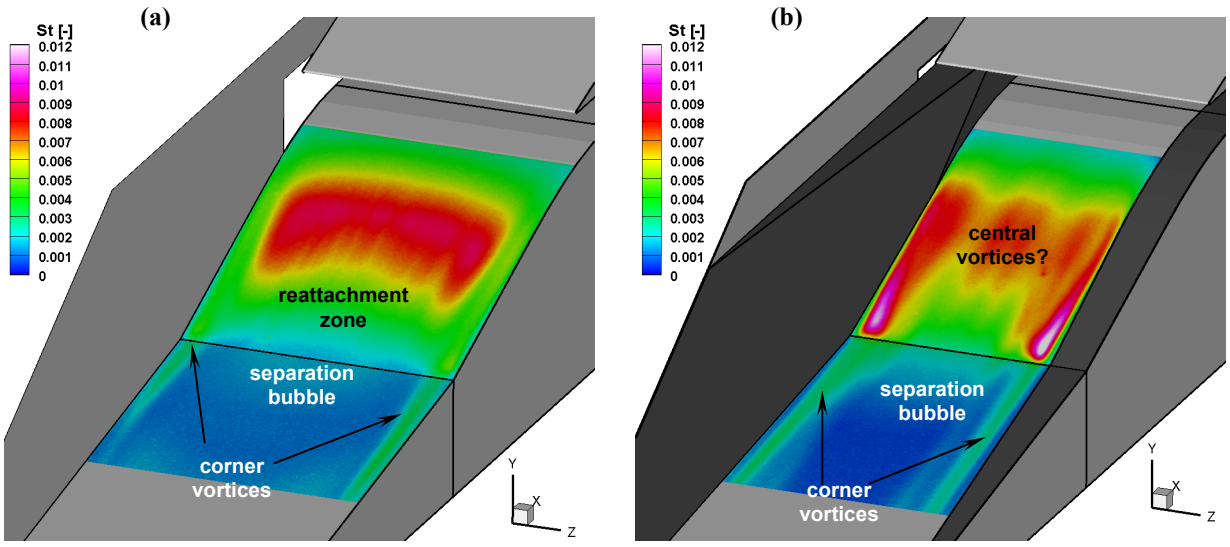

Figure 7. St-number distribution on external for a) configuration without inserts and b) configuration with 70 mm external sidewall compression inserts

The flow turns turbulent in the shear layer over the separation bubble, resulting in higher heat loads on the second ramp after the flow has reattached. Furthermore, the areas with higher St-numbers close to the sidewalls on the first ramp indicate the presence of corner vortices. Due to the difficulty of finding a scale at which most of the flow phenomena can be visualized, these are not very distinct.

In the case with 70 mm sidewall compression inserts, these corner vortices already appear a little stronger on the first ramp. The interaction with the second ramp shock strongly amplifies these vortices resulting in a very high increase of the St-number in this area. Stainback and Weinstein already noted the importance of heating caused by corner vorticity in the design of hypersonic vehicles [25]. The results from the current measurement campaign show, that in the case of 3D-inlets, even more attention has to be paid to this aspect.

In the central part of the second ramp, the IR-measurements show slightly higher and more heterogeneous heat flux distribution. This is a result of the three-dimensional flow created by the interaction of the core flow and the corner flow. It does appear as there are some vortex structures present here but there are considerable discrepancies between the measurements and the CFD-calculations by Nguyen [23] so it remains very uncertain how the flow structure actually looks like. It is especially unsure, how the sidewall compression influences the transitional behaviour. Additional windtunnel runs are planned for the future, using oilfilm images to visualize the flow structure on the ramp surfaces. Hopefully this will give more insight and allow for better agreement of computations and experiments.

Overall, because of the flow structure on the external ramps and the consequential poor starting behaviour, the combination of a double-ramp inlet and sidewall compression seems very unfavourable.

B. Performance

Figure 1 shows the comparison of the mass flow rates for all the different configurations and lip positions. The results show that a strong reduction of the spillage mass flow can be achieved by the adaption of the lip position. In the case without sidewall inserts, it was possible to capture almost the full mass flow through the capture are when the lip was extended to x=340 mm. With external sidewall compression, the MCR also can be increased but is limited by the point at which the inlet does not start anymore. For additional internal contraction, the results look very similar than those of the 2D-case. There is no difference in between the two different insert configurations but the values are slightly lower than in the 2D-case. It is believed that this is due to an upstream effect of the internal

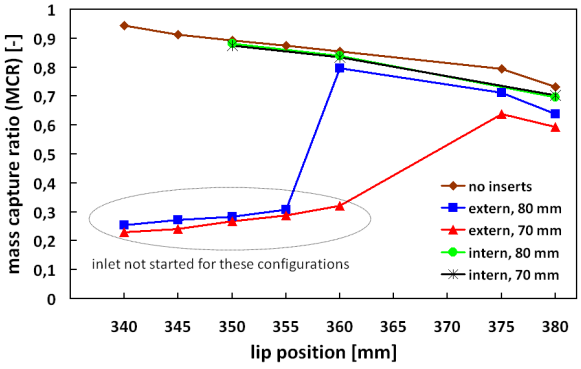

Figure 8. Mass capture ratio for all configurations

sidewall compression wedges along the upper wall, as it was also noticed by Häberle [14]. The wall pressure distribution, discussed in the next section and illustrated in Figure 10, is also effected by this.

The comparison of both the static and total pressure ratios of the different configurations is shown in Figure 9. It illustrates that a considerable increase of the static pressure ratio by the elongation of the lip and consequential higher MCR by itself cannot be achieved – the static pressure ratio is only increased by about 11 %. On the other hand, in combination with additional sidewall compression, much higher pressure levels can be achieved although the starting behaviour of the cases with external sidewall compression acts as a limiting factor. In the case of additional internal sidewall compression with reduction of the throat width to 80 mm, the strongest gains in the static pressure level can be achieved, yielding an increase of more than 50 %. However, for the 70 mm inserts, the increase is much smaller, although it would be expected to be higher due to larger compression angles of the inserts.

Regarding the total pressure ratio, displayed in Figure 9 (b) the results are mostly as expected. For the basic lip length of 380 mm, the total pressure ratios of the external compression is higher than for the internal compression because of the smaller compression angles and resulting weaker shocks. However, it is still lower than in the 2D-case. The total pressure recovery increases when the cowl lip is extended to the front. The increases for all configurations with sidewall compression are lower than in the 2D-case. This presumably due to the fact, that the second ramp shock is going underneath the cowl and interacting with the lip shock before it hits the cowl.

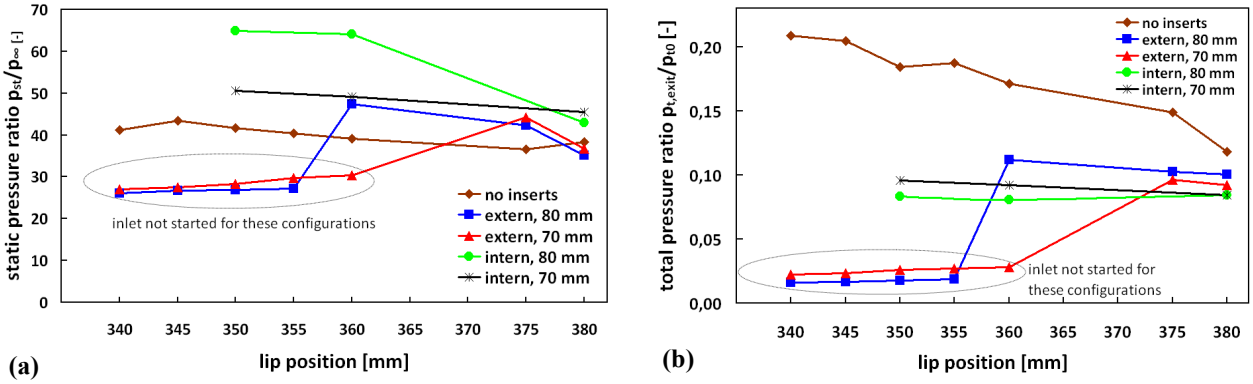

Figure 9. Comparison of (a) static and (b) total pressure ratios for all configurations

C. Flowfield

1. Comparison of different insert configurations

Figure 10 shows the static pressure distribution along the centreline of the upper and lower wall of the inlet up to the defined interface of the inlet/isolator part and the combustion chamber of the different insert configurations for a lip position of x = 380 mm. The additional external sidewall compression does not yield significant changes in the pressure levels (the results for the reduction of the throat width from 100 mm to 70 mm by external sidewall compression are omitted, as they barely differ from the case with 80 mm throat width). However, the inserts for internal sidewall compression cause a strong pressure rise in the isolator part in the region from x = 490 – 550 mm by a factor of up to3 for the 70 mm case. As previous investigations already showed that the isolator was designed too long by about one third [15], the section of the isolator showing the strongest pressure rise would actually be the one where the interface of the combustion chamber should be, and consequently these types of inserts would cause a pressure rise in the area where fuel injection and ignition should take place. Downstream of this area, however, the pressure level aligns with the one of the 2D-case again.

The current examinations also show a strong upstream effect for the cases with internal sidewall compression. The strong pressure rise in the throat area, in the area between x = 0.38 m and 0.44 m, which starts clearly ahead of the leading edge of the sidewall inserts at x = 0.41 m. This is due to the interaction of the shocks that are induced by the sidewall compression wedges with the boundary on both the upper and lower wall. This effect has also already been observed in previous investigations [15]. The interaction of these shocks with the boundary layer on the lower wall causes the separation bubble on the expansion surface of the lower wall to move upstream which can be seen by the pressure rise in the region around x = 370 mm. Consequently the separation shock hits the upper wall further upstream as well, thus causing the strong increase in pressure at the first pressure port of the upper wall.

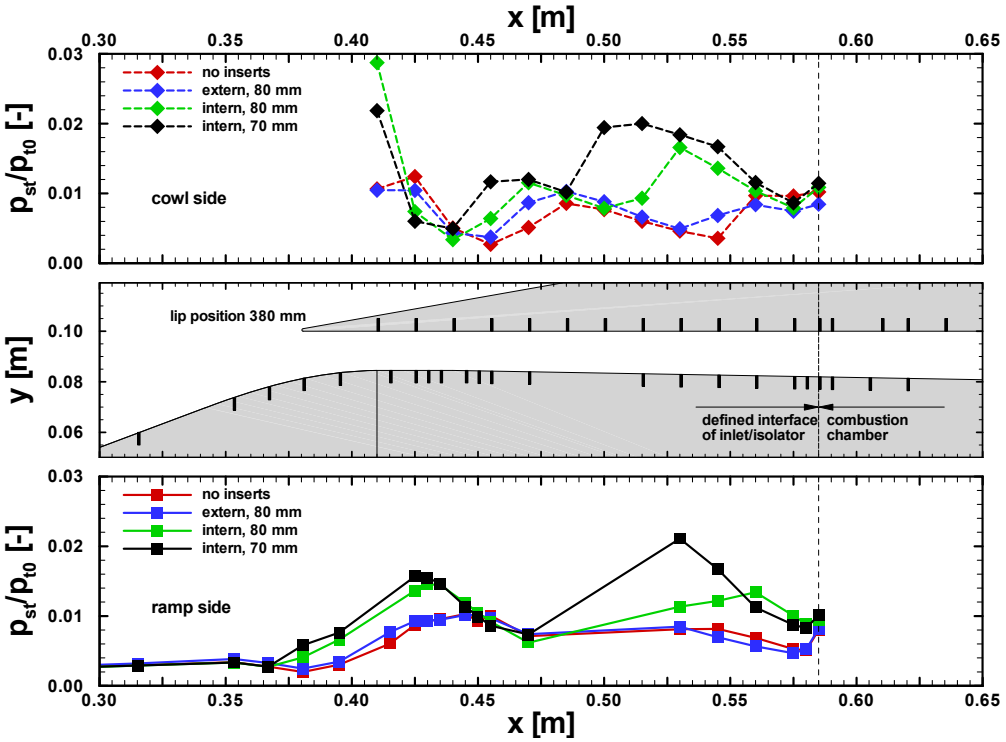

Figure 10. Wall pressure distribution for different insert types for lip position x = 380 mm.

Overall, it is expected that the addition of sidewall compression creates a more inhomogeneous flowfield by introducing more three dimensional effects to flow. However, the plots of Pitot pressure and Mach number distribution over the isolator height in Figure 11 indicate that in the y-direction, the flow is more homogeneous than in the 2D-case. The variation of both Pitot pressure and Mach number over the isolator height is much smaller. The configuration of 70 mm internal compression shows the smallest variation of both parameters. Furthermore, the

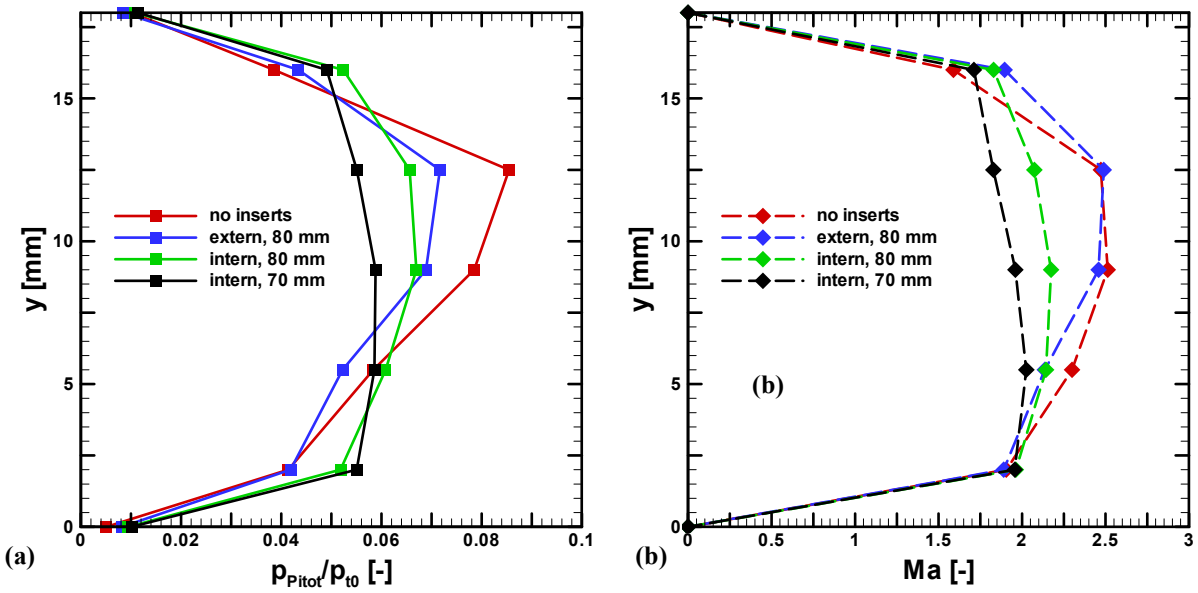

Figure 11. Distribution of (a) Pitot pressure and (b) Mach number over the isolator height for lip position x = 380 mm

Mach number is lowest for this configuration. For the Pitot pressure, the peak value is much lower, but close to the walls, the Pitot pressure is higher than for the 2D-case. The profiles for external sidewall compression are more similar to the 2D-case. Especially the Mach number distribution is almost equal. The Pitot pressure distribution shows a lower level in the centre part of the isolator, but the characteristics are very similar. Like for the wall pressure distribution, the profiles for the two different throat widths for external sidewall compression are almost identical.

In order to check, how the 3D-inserts influence the flow structure in the span wise direction, the Pitot rake was moved 25 mm off the centreline towards the wall. Figure 12 shows the comparison of the Pitot pressure profiles on and off the centreline for the different insert types.

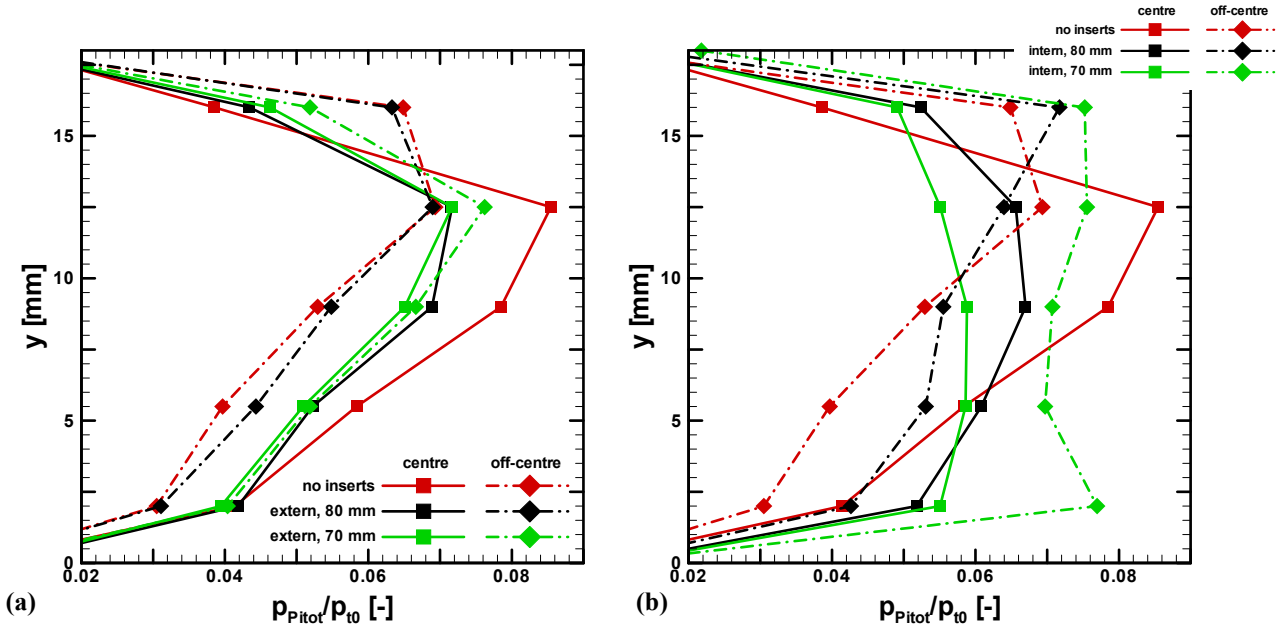

Figure 12. Comparison of centreline and off-centreline Pitot pressure profiles for (a) external and (b) internal sidewall compression

For external sidewall compression, it is very interesting to note that the flow becomes more homogeneous as the sidewall compression is increased. The discrepancies between the profile on and off the centreline are largest for the 2D-case. For 80 mm compression, the off-centreline profile is nearly identical to the 2D-case but does not differ as much from the centreline profile. Finally, 70 mm there are only very small differences between the two different locations of the Pitot rake. Since the converging part of the external sidewall inserts already ends in the area of the cowl lip, it appears that the 3D-shock structures that are induced by the inserts do not protrude into the isolator and that the flow is very much homogenized.

Opposed to that, for internal compression, the 3D-shock structures are only introduced in the isolator part of the inlet. Therefore, the flow is still very non-uniform in the z-direction at the interface to the combustion chamber (where the Pitot rake is located). For the 80 mm inserts, the tendency is similar to the one in the 2D-case: The Pitot pressure at top Pitot tube is increased while it decreases at all other places, although the quantitative changes are smaller. Reducing the width to 70 mm results in much larger changes. The Pitot pressure rises at all Pitot tubes, and the highest value is now measured at the Pitot tube closest to the bottom whereas it was at the topmost one for the other two configurations. However, the differences of the Pitot pressure at the different Pitot tubes are now smaller. A clearer interpretation of these results would require a better characterization of the internal flow field, which, however, is very challenging.

To see the influence of the lip position, and consequently higher captured massflow, on the internal flowfield of the various configurations, the wall pressure distribution of the different configurations for a lip length of x = 360 mm is displayed in Figure 13.

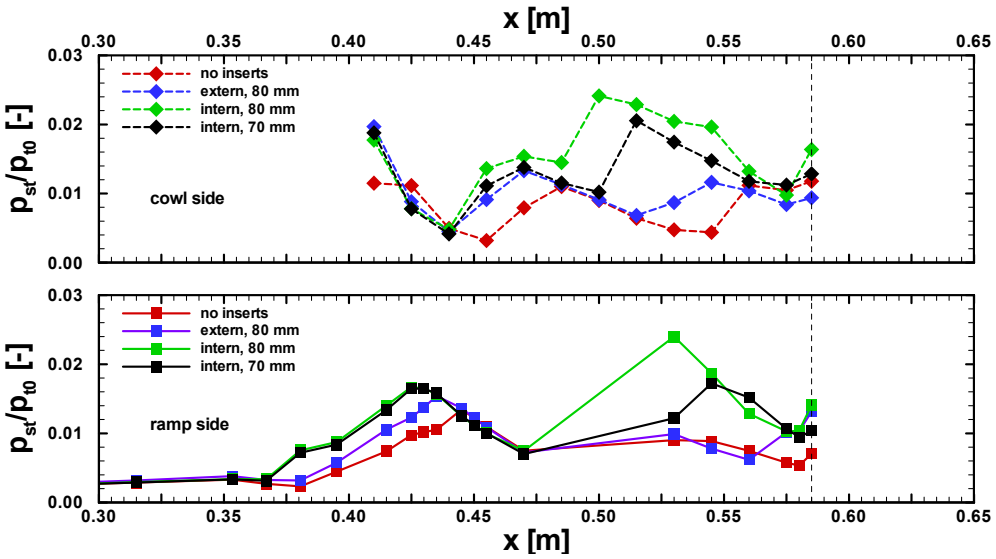

Figure 13: Wall pressure distribution for different insert types for lip position x = 360 mm

The profiles show one surprising effect: The highest values were measured for the configuration of 80 mm internal compression, although the compression angles of this case are smaller than in the 70 mm case. Especially along the lower wall, the values are much higher. The peak value along the upper wall for both configurations with internal compression is moved upstream, but occurs sooner in the 80 mm case. Due to the elongation of lip, the shock structure is moved as well. Since due to constructive reason there are no pressure ports along the lower wall in the region, it is not known whether this occurs along the lower wall as well. The pressure rise for the configurations with internal sidewall compression in the throat section is caused by the upstream effect due to the interaction that was already mentioned above.

For the case of external sidewall compression, a pressure rise can be noted in the throat section. Furthermore, the increase of pressure along the upper wall in the downstream part of the isolator is more distinct than for the 380 mm lip.

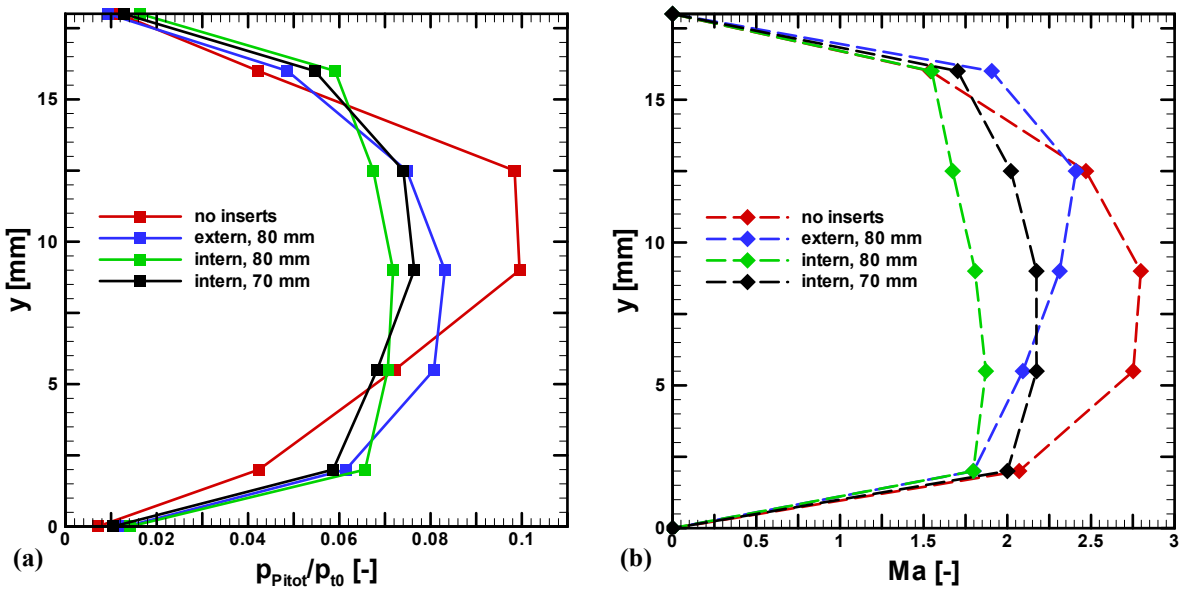

Figure 14. (a) Pitot pressure and (b) Mach number profiles for lip position x = 360 mm

Regarding the Pitot and Mach number profiles, which are shown in Figure 14, also for this lip length the flow seems to become more homogeneous by the addition of internal sidewall compression. The Mach number and Pitot pressure levels of the 80 mm case are lower than for the 70 mm case which corresponds to the observations made from the wall pressure distribution. Again, the highest values are achieved for the 2D-case, however, the location of the peak value has moved to the lower wall, corresponding to the movement of the shock structure by the elongation of the lip. In the case of external compression, the profiles now differ substantially from the 2D-case.

2. Comparison of different lip lengths

In this section, the influence of the lip lengths on the flowfield is analyzed more closely. By elongating the lip to the front, the internal contraction ratio is significantly increased, as described in section II. Only the 2D-configuration is used for this, because only for this configuration, a full set of data for all lip length is available and it was possible to take shadowgraph images. Figure 15 shows the comparison of the static pressure distribution along the lower and upper wall of the inlet for different lip positions for the configuration without sidewall compression inserts as well as shadowgraph images for lip position of x = 380 mm and x = 340 mm. The shadowgraph images of the first window show the changes in the shock structure very well, when the lip is extended

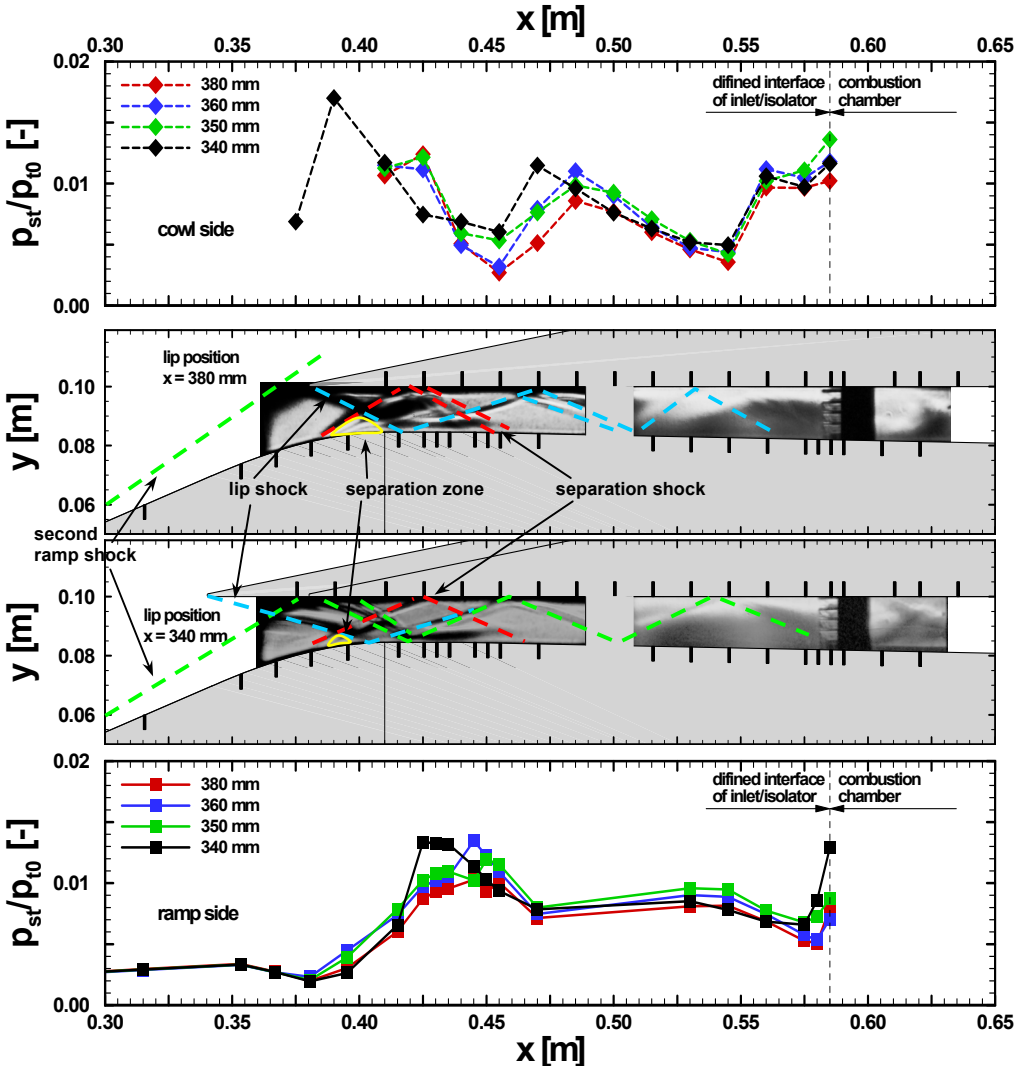

Figure 15. Wall pressure distribution and shadowgraph images for different lip lengths for configuration without inserts

from x = 380 mm to x = 340 mm. In the original lip position, the second ramp shock passes clearly ahead of the cowl lip. The interaction of the lip shock with the ramp boundary layer causes a separation bubble in the throat in between x = 390 and 410 mm. The separation shock in turn causes the boundary layer on the upper wall to separate at about x= 420 mm. The size of this separation zone is much smaller, however. The reattachment shock of the separation bubble on the lower wall is reflected in a shock-train like structure throughout the length of the isolator. The separation and reattachment shocks of the separation zone on the upper wall are much weaker and are not visible anymore after interacting with the ramp boundary layer.

If the lip is elongated by more than 5 mm, the shock from the second ramp is swallowed by the cowl lip. It first interacts with the lip shock and then hits the upper wall at about the place of the second pressure port, i.e. at about x= 375 mm. The shock produces only a small separation zone at the upper wall. The separation and reattachment shocks only interact with the ramp boundary layer after the separation region that is caused by the interaction with the lip shock. This separation region still starts at about the same location x = 390 mm but is much smaller, only extending to about x = 400 mm. In this case, the separation shock of this separation zone appears much weaker, and after it is reflected by the upper wall and hits the lower wall again, it can not be noted anymore in the shadowgraph images. On the other hand, both the reattachment and separation shocks of the separation zone induced by the second ramp shock can be seen to be reflected throughout the length of the isolator in the same way it was the case with the reattachment shock from the separation bubble on the lower wall for the 380 mm lip. The shock structure is also still at almost the same position, therefore also no shift in the pressure profiles along both the upper and low wall can be identified.

Although, as Figure 8 illustrates, the mass flow is increased by almost 30% due to the elongation of the lip, an overall increase of the static pressure level from the extension of the lip cannot be observed. There is a strong pressure rise in the leading part of the cowl for those configurations where the second ramp shock hits the cowl. The changes in the shock structure also cause an increase of the pressure along the lower wall in the throat section. However, in the rear part of the isolator, the flow becomes more homogeneous again and the pressure characteristics of the different configurations become more alike.

The changes in the Pitot pressure that are induced by the extension of the lip are much greater. As shows, there is strong increase in the Pitot pressure in the centre part of the isolator, while the differences are small at the Pitot tubes close to the wall. Interesting to note is that the location at which the peak Pitot pressure is reached, changes several times when the lip is extended further (this is also true for the configurations not displayed here). The change of the lip position from 360 mm to 350 mm causes a strong increase in Pitot pressure in the upper half of the isolator flow while the pressure falls in the lower part. The further extension to 340 mm shows the exact opposite, a strong increase in the lower and centre part of the flow, but a decrease in the upper part. This always a sign of lateral movements of the shock structures in the isolator which is due to the change of the location of the lip shock and the resulting change in the interaction with shocks from the separation bubble on the ramp expansion surface.

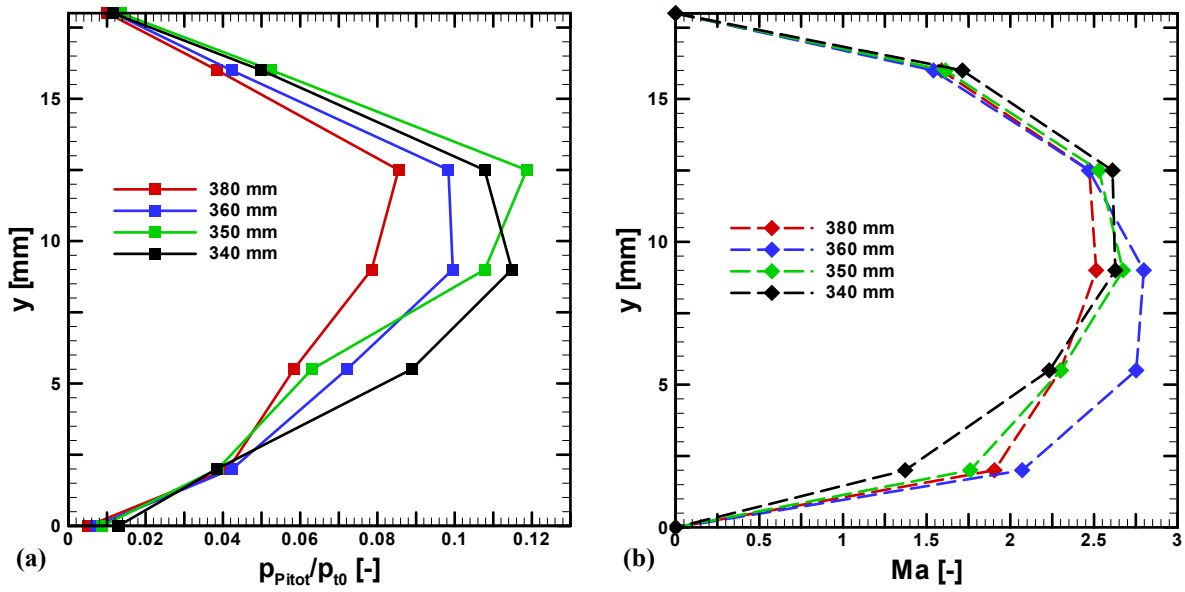

Figure 16. Pitot pressure (a) and Mach number (b) profiles for different lip lenghts for the 2D-configuration

V. Conclusion

The results of this experimental campaign gave lots of insight into aspects that have to be considered in the design of three-dimensional inlets. For once, it is shown again that the Kantrowitz-Limit is only a weak criterion to judge on the starting behaviour of hypersonic inlets. Much more attention has to be paid to the flow structure and the property occurring in the respective configurations such as vortex structures, shock-shock and shock-boundary layer interaction and separation. For the inlet configuration that was investigated in the present study, the combination of a two-ramp inlet with swept sidewall compression wedges for external sidewall compression proved to be very unfavourable as strong separation and vortex structures were induced on the external ramps. This had very negative effect on the starting behaviour. Because of this, it was possible to adapt the lip appropriately to reduce the spillage, which is strongly increased by the interaction of the ramp and sidewall shocks. This also inhibited any improvements of the static pressure in the isolator by this type of sidewall compression.

Opposed to this, significant increase of the compression ratio of the inlet was achieved by additional internal sidewall compression. The static pressure could almost be tripled in certain areas, and the overall static pressure ratio could be raised by almost 70%. At the same time, it was possible to capture significantly more mass flow by adapting the lip position. In this configuration, as well as in the 2D-case, it was possible to elongate the lip quite far upstream without inhibiting the self-starting of the inlet. The internal contraction ratios in these cases were well above the Kantrowitz-Criterion. Furthermore, the movement of the second ramp shock and its interaction with the boundary layer on the cowl and the separation caused there do not have negative influence on this.

Overall, it seems that the starting behaviour is more influenced by the flow in the external part of an inlet, than by the internal contraction. Therefore, additional experiments are planned for the future to investigate the external flowfield more closely. To do so, oilfilm images will be used to visualize the flow structure on the surfaces of the external ramps which hopefully will give more insight into the shock-shock and shock-boundary layer interaction as well as the vortex structures.

Acknowledgements

We would like to thank the German Research Foundation DFG for their funding of this project within the frame of the research training group GRK 1095/2 “Aero-Thermodynamic Design of a Scramjet Propulsion System for Future Space Transportation Systems”. Special thanks also go to Florian Klingenberg and Manuel Schorn for jumping in as operating team of the H2K and performing really good wind tunnel runs although it was their first time operating this tunnel. But of course, also thanks to Michael Kosbow and Marco Schmors, the regular operating team of H2K, for performing some of the wind tunnel runs as reliable as always.

References

[1] Weigand, B., Gaisbauer, U., Reinartz, B., Kau, H.-P., and Schröder, W., Das Graduiertenkolleg 1095/1: "Aero-thermodynamische Auslegung eines Scramjet-Antriebssystems für Zukünftige Raumtransportsysteme", *DGLR-Paper*, 2006-127, 2006.

[2] Gruhn, P., Wind Tunnel Tests with Modified LC01k Intake, LAPCAT II Deliverable D4.1.1, ACP7-GA-2008-21 1485, Cologne, Germany, January 2010.

[3] Heiser, W. H. and Pratt, D. T., *Hypersonic Airbreathing Propulsion*, AIAA Education Series, Washington, DC, 1st ed., 1994.

[4] Häberle, J. and Gülhan, A., Internal Flowfield Investigation of a Hypersonic Inlet at Mach 6 with Bleed, *Journal of Propulsion and Power*, Vol. 23, No. 5, September-October 2007, pp. 1007–1017.

[5] Henckels, A. and Gruhn, P., Experimental Optimisation of Intake and Sensitivity Analysis of Perturbations on Intake Performance in H2K, *LAPCAT Report*, Vol. AST4-CT-2005-012282, No. D.7.1.1, March 2008.

[6] Henckels, A. and Gruhn, P., Study on Aerothermal Effects of Viscous Shock Interaction in Hypersonic Inlets, *Proceedings of the Fifth European Symposium on Aerothermodynamics for Space Vehicles*, ESA SP-563, Cologne, February 2005.

[7] Triesch, K., Ebener Scramjeteinlauf SCR1 (Aufbau der Innenströmung und Einfluss der Einspritzelemente), *DLR Interner Bericht*, Vol. IB 39113-2000 C03, February 2000.

[8] Holland, S. D., Mach 10 Computational Study of a Three-Dimensional Scramjet Inlet Flow Field, *NASA Technical Memorandum*, Vol. TM 4602, March 1995.

[9] Holland, S. D., Mach 10 Experimental Database of a Three-Dimensional Scramjet Inlet Flow Field, *NASA Technical Memorandum*, Vol. 4648, September 1995.

[10] Goonko, Y. P., Kharitonov, A. M., Mazhul, I. I., Zvegintsev, V. I., Nalivaichenko, D. G., and Chirkashenko, V. F., Investigation of a Scramjet Model at Hypersonic Velocities and High Reynolds Numbers, *AIAA*, Vol. 2002-5273, 2002.
[11] Goonko, Y. P., Latypov, A. F., Mazhul, I. I., Kharitonov, A. M., Yaroslavtsev, M. I., and Rostand, P., Structure of Flow over a Hypersonic Inlet with Side Compression Wedges, *AIAA Journal*, Vol. 41, No. 3, March 2003, pp. 436–447.
[12] Smart, M. K., Design of Three-Dimensional Hypersonic Inlets with Rectangular-to-Elliptical Shape Transition, *Journal of Propulsion and Power*, Vol. 15, No. 3, May-June 1999, pp. 408–416.
[13] Smart, M. K., Experimental Testing of a Hypersonic Inlet with Rectangular-to-Elliptical Shape Transition, *Journal of Propulsion and Power*, Vol. 17, No. 2, March-April 2001, pp. 276–283.
[14] Häberle, J. and Gülhan, A., Experimental Investigation of a Two-Dimensional and a Three-Dimensional Scramjet Inlet at Mach 7, *Journal of Propulsion and Power*, Vol. 24, No. 5, September-October 2008, pp. 1023–1034.
[15] Häberle, J., Untersuchungen zum Externen und Internen Strömungsfeld eines Scramjet Triebwerkseinlaufs bei Unterschiedlichen Betriebspunkten, *DLR Forschungsbericht*, ISRN DLR-FB–2009-14, 2009.
[16] Niezgodka, F.-J., Der Hyperschallwindkanal H2K des DLR in Köln-Porz (Stand 2000), *DLR Mitteilung*, 2001-01, January 2001.
[17] Anderson, B. H., Design of Supersonic Inlets by a Computer Program Incorporating the Method of Characteristics, *NASA Technical Note*, TN-D-4960, January 1969.
[18] Häberle, J. and Gülhan, A., Investigation of Two-Dimensional Scramjet Inlet Flowfield at Mach 7, *Journal of Propulsion and Power*, Vol. 24, No. 3, May-June 2008, pp. 446–459.
[19] Kantrowitz, A. and duP. Donaldson, C., Preliminary Investigation of Supersonic Diffusors, *NACA Wartime Report*, ACR L5D20, May 1945.
[20] Triesch, K. and Krohn, E.-O., Verwendung von Kegeldüsen zur Drosselung und Durchsatzmessung bei Überschalleinläufen, *DFVLR-Bericht*, IB-39113-83-A-04, 1984.
[21] DIN Deutsches Institut für Normung e.V., *Durchflußmessung mit Blenden, Düsen und Venturirohren in voll durchströmten Rohren mit Kreisquerschnitt*, DIN 1952 (VDI Durchflussmeßregeln), July 1982.
[22] FLIR Systems, *ThermaCAM SC-3000*, Users Manual.
[23] Nguyen, T., Behr, M., Reinartz, B., Hohn, O., and Gülhan, A., Numerical Investigations of the Effects of Sidewall Compression and Relaminarization in 3D Scramjet Inlet, *17th AIAA International Space Planes and Hypersonic Systems and Technologies Conference*, San Francisco, AIAA-Paper 2011-2256, April 2011.
[24] Neuenhahn, T. and Olivier, H., Numerical Study of Wall Temperature and Entropy Layer Effects on Transitional Double Wedge Shock Wave/Boundary Layer Interactions, *26th International Symposium on Shock Waves*, July 15 - 20 2007.
[25] Stainback, P. C. and Weinstein, L. M., Aerodynamic Heating in the Vicinity of Corners at Hypersonic Speeds, *NASA Technical Note*, TN-D-4130, 1967.